Influence of vortex dynamics and structure on turbulence statistics at large scales

Cite as: Phys. Fluids **27**, 055106 (2015); https://doi.org/10.1063/1.4921210
Submitted: 29 December 2014 . Accepted: 05 May 2015 . Published Online: 19 May 2015

Katsunori Yoshimatsu, Koujiro Anayama, and Yukio Kaneda

PHYSICS OF FLUIDS **27**, 055106 (2015)

Influence of vortex dynamics and structure on turbulence statistics at large scales

Katsunori Yoshimatsu,[1,a)] Koujiro Anayama,[2] and Yukio Kaneda[3]
[1]*EcoTopia Science Institute, Nagoya University, Nagoya 464–8603, Japan*
[2]*Department of Computational Science and Engineering, Nagoya University, Nagoya 464–8603, Japan*
[3]*Aichi Institute of Technology, 1247, Yachikusa, Yakusacho, Toyota 470-0392, Japan*

(Received 29 December 2014; accepted 5 May 2015; published online 19 May 2015)

The question whether the vortex dynamics and structure at small scales have significant influence on the statistics at large scales is addressed on the basis of quantitative comparison of two turbulent fields. One is a reference field generated by direct numerical simulation of turbulence of an incompressible fluid obeying the Navier-Stokes (NS) equation in a periodic box. The other is an artificial field in which the coherent vortical structures at small scales ($\sim\eta$) that could be formed by the NS dynamics in the reference field are destroyed by an artificial computational operation, where η is the Kolmogorov micro-length scale. The comparison of the two fields suggests that the statistics at larger scale ($\gg\eta$) are not sensitive to the exact vortex dynamics and structure, at least in the case studied here. © *2015 AIP Publishing LLC.* [http://dx.doi.org/10.1063/1.4921210]

I. INTRODUCTION

One of the most characteristic features of three-dimensional (3D) turbulence is the existence of the vortex dynamics, such as the vortex stretching by which intense vortex field is generated. The vortex dynamics and structure are often regarded in the literature to be very important and fundamental elements in turbulence dynamics. In fact, extensive studies have been made on them.

On the other hand, most vorticity in fully developed turbulence at high Reynolds number resides at small scales in the so-called energy dissipation range, while most turbulent kinetic energy is at the scales in the so-called energy containing range, that is at scales much larger than those in the dissipation range. Studies so far made suggest that a certain class of statistics of turbulence is not so sensitive to the exact dynamics or structure in the dissipation range. For example, the normalized average of the energy dissipation rate per unit mass at very high Reynolds number is almost determined only by the characteristic length and velocity of the energy containing range, but independent of the viscosity.[1] It is also to be noted that, as is briefly reviewed in Sec. II, the Kármán-Howarth-Kolmogorov (KHK) equation[2] suggests that under certain conditions, the third-order longitudinal structure function in the inertial subrange is determined irrespectively of the details of the dynamics, structures, morphology, deformation, collisions process, etc., of small eddies at the dissipation range. These considerations suggest that the exact dynamics and structures at small scales in the dissipation range play only a secondary role in the determination of a certain class of statistics at larger scales.

One may then ask whether the dynamics and structures at small scales have significant influence on the statistics at large scales. Is it significant? In this paper, this question is addressed by comparing two kinds of fields. One is a reference field generated by direct numerical simulation (DNS) of turbulence of an incompressible fluid obeying the Navier-Stokes (NS) equation under periodic boundary condition and external forcing confined to large scales. The other is generated

a)yoshimatsu.katsunori@g.mbox.nagoya-u.ac.jp

by an artificial computational operation, called computational surgery, by which the small-scale dynamics and structures are destroyed so that the coherent structures that could be formed by the NS dynamics in the reference field are lost or significantly disturbed. The comparison of the two fields may give some idea on how important or unimportant is the broken dynamics or the lost structures on statistics at larger scale.

II. METHODS OF SIMULATION AND COMPUTATIONAL SURGERY

A. Basic equations

We consider 3D motion of an impossible fluid obeying the NS equation

$$\frac{\partial \boldsymbol{u}}{\partial t} + (\boldsymbol{u}\cdot\nabla)\boldsymbol{u} = -\frac{1}{\rho}\nabla p + \nu\nabla^2\boldsymbol{u} + \boldsymbol{f} \tag{1}$$

and the incompressibility condition

$$\nabla\cdot\boldsymbol{u} = 0, \tag{2}$$

where $\boldsymbol{u} = \boldsymbol{u}(\boldsymbol{x},t)$ is the velocity, $p = p(\boldsymbol{x},t)$ the pressure, $\boldsymbol{f} = \boldsymbol{f}(\boldsymbol{x},t)$ the external force, ν the kinematic viscosity, ρ the density, t the time, $\boldsymbol{x} = (x_1, x_2, x_3)$ the position, and $\nabla = (\partial/\partial x_1, \partial/\partial x_2, \partial/\partial x_3)$. Here and hereafter, we omit the arguments $\boldsymbol{x}$ and t at will.

Let us briefly review here, along the line of Kaneda and Morishita,[3] the implication of the two fundamental exact equations for homogeneous and isotropic turbulence of incompressible fluid obeying the NS equation.

One of the two fundamental exact equations is the KHK equation

$$B_3^L(r) = -\frac{4}{5}\langle\epsilon\rangle r + 6\nu\frac{\partial B_2^L(r)}{\partial r} + F(r) - \frac{3}{r^4}\int_0^r \frac{\partial B_2^L(\tilde{r})}{\partial t}\tilde{r}^4 d\tilde{r}. \tag{3}$$

Here, $\langle\epsilon\rangle$ is the average of the rate of energy dissipation ϵ per unit mass, $r = |\boldsymbol{r}|$ is the separation distance vector between two points $\boldsymbol{x}$ and $\boldsymbol{x}+\boldsymbol{r}$, and $B_n^L(r)$ is the nth-order structure function of the longitudinal velocity difference δu^L, defined as

$$B_n^L(r) \equiv \left\langle (\delta u^L)^n \right\rangle, \tag{4}$$

where the brackets $\langle\ \rangle$ denote the ensemble average, and $\delta u^L \equiv \{\boldsymbol{u}(\boldsymbol{x}+\boldsymbol{r}) - \boldsymbol{u}(\boldsymbol{x})\}\cdot(\boldsymbol{r}/r)$. The average may be regarded as the spatial average for homogeneous turbulence. The term $F(r)$ in Eq. (3) is due to the forcing $\boldsymbol{f}$ and is given by

$$F(r) = \frac{6}{r^4}\int_0^r \tilde{r}G(\tilde{r})d\tilde{r},$$

where

$$G(r) = \int_0^r \tilde{r}^2 g(\tilde{r})d\tilde{r}$$

and

$$g(r) \equiv \langle[\boldsymbol{u}(\boldsymbol{r}+\boldsymbol{x}) - \boldsymbol{u}(\boldsymbol{x})]\cdot[\boldsymbol{f}(\boldsymbol{r}+\boldsymbol{x}) - \boldsymbol{f}(\boldsymbol{x})]\rangle.$$

Like $B_n^L(r)$, $g(r)$ too is independent of the direction of $\boldsymbol{r}$ in isotropic turbulence.

The other is the equation for the energy spectrum $E(k)$, or the so-called Lin equation,

$$\frac{\partial E(k)}{\partial t} = T_E(k) - 2\nu k^2 E(k) + F_E(k), \tag{5}$$

where $E(k)$ is so normalized that $E = \int E(k)dk = 3u'^2/2$, in which u' is the root-mean-square of the fluctuating velocity in one direction, k is the wavenumber, and E is the total turbulence kinetic energy per unit mass while $T_E(k)$ represents the energy transfer function due to the nonlinear interaction and $F_E(k)$ is the energy input due to the forcing $\boldsymbol{f}$.

The integration of Eq. (5) with respect to k from K to ∞ and the replacement of K to k give

$$\Pi(k) = \langle\epsilon\rangle - 2\nu \int_0^k p^2 E(p)dp - \int_k^\infty F_E(p)dp + \int_k^\infty \frac{\partial E(p)}{\partial t}dp, \tag{6}$$

where $\Pi(k)$ is the energy flux across the wavenumber k defined by

$$\Pi(k) \equiv -\int_0^k T_E(p)dp,$$

and we have used

$$\int_0^\infty T_E(k)dk = 0 \quad \text{and} \quad \langle\epsilon\rangle = 2\nu \int_0^\infty k^2 E(k)dk.$$

If the force $\boldsymbol{f}$ is only at large scales, say $\sim L$, and the viscosity ν is very small, then it is plausible to assume that in Eq. (3),

(i) the forcing term $F(r)$ is negligibly small at $r \ll L$ and
(ii) the viscosity term, i.e., the second term in the right-hand side of Eq. (3) works only at the small scales $\sim\eta$ in the dissipation range, so that it is negligibly small at $r \gg \eta$.

Here, η is the Kolmogorov micro-length scale defined by $\eta \equiv (\nu^3/\langle\epsilon\rangle)^{1/4}$. Under these assumptions and (iii) the assumption of statistical stationarity, Eq. (3) yields the 4/5 law,

$$B_3^L(r) = -\frac{4}{5}\langle\epsilon\rangle r, \tag{7}$$

for $L \gg r \gg \eta$, which is called here the inertial subrange.

Under the assumptions similar to (i) and (ii), i.e.,

(i') the forcing term $F_E(k)$ is negligibly small at the wavenumber range $k \gg K_L \equiv 1/L$,
(ii') the viscosity term, i.e., the second term in the right-hand side of Eq. (6), is negligibly small at $k \ll k_\eta \equiv 1/\eta$,

and (iii) the assumption of the statistical stationarity, Eq. (6) gives

$$\Pi(k) = \langle\epsilon\rangle \tag{8}$$

for $1/L \ll k \ll 1/\eta$. Relation (8) is equivalent to 4/5 law (7). Readers may refer to Frisch[4] for some details on the relation between Eqs. (7) and (8).

The KHK equation and the Lin equation imply that the third-order moments $B_3^L(r)$ and the energy transfer $\Pi(k)$ are given by Eqs. (7) and (8), irrespectively of the detail of the forcing at large scales ($\sim L$), nor the details of eddies or their motions, such as their morphology, deformation, coagulations, and collisions, at the small scales ($\sim\eta$), as far as assumptions (i), (ii) (or (i') and (ii')), and (iii) are satisfied. Thus, the equations suggest that the role of the exact vortex dynamics and structure at the small scales on larger-scale turbulent statistics ($\gg\eta$) is limited in this sense.

Note that if one may assume that the r-dependence of the skewness of δu^L is weak, then one can derive from Eq. (7) the r-dependence of the 2/3 power law for $B_2^L(r)$, as noted by Kolmogorov.[2]

B. Method of simulation and computational surgery

In this study, we consider two kinds of fields. One is a reference field; a forced turbulent field simulated by solving Eqs. (1) and (2) in a periodic box of fundamental length 2π in each of the Cartesian coordinate directions. We use the so-called negative viscosity model (see, e.g., Ref. 5) for the forcing $\boldsymbol{f}$, which is consistent with assumptions (i) and (i'), and given by

$$\hat{\boldsymbol{f}}(\boldsymbol{k}) = \begin{cases} c(t)\hat{\boldsymbol{u}}(\boldsymbol{k}) & (\text{for } k < k_F), \\ 0 & (\text{otherwise}), \end{cases} \tag{9}$$

where $\hat{\cdot}$ denotes the Fourier transform of $\cdot$, k_F is a prescribed threshold value, which was put to be 2.5 in our simulation, $c(t)$ is a non-negative constant independent of the wave vector $\boldsymbol{k}$ so adjusted

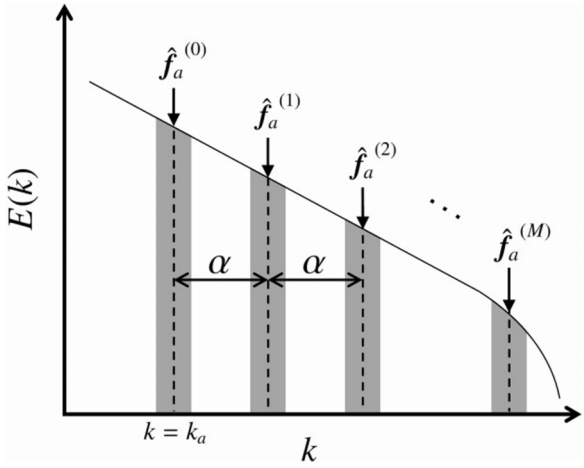

FIG. 1. A sketch of the input by the artificial forcing $\boldsymbol{f}_a$.

at each time step that the total kinetic energy E is constant (=0.5) independent of time, and $k = |\boldsymbol{k}|$. Note that the energy input through this forcing is only at low wavenumber modes, i.e., only at large scales, and the forcing has no direct influence to the Fourier modes with $k > k_F$. We call here this field "true field" or "T-field."

The other field is obtained by simulation with introducing an artificial computational operation, which we call here "computational surgery," to the T-field. We call here this field "false field" or "F-field." The operation is applied so as to destroy or interrupt the formation of coherent structures, such as tube-like vortex structures, at small scales ($\sim\eta$), which could be formed by the NS dynamics in the T-field. The operation is applied only at the small scales, in contrast to the large-scale forcing $\boldsymbol{f}$. The operation is expressed as an addition of an artificial forcing, say $\boldsymbol{f}_a$ to Eq. (1), i.e., by replacing $\boldsymbol{f}$ in Eq. (1) to $\boldsymbol{f} + \boldsymbol{f}_a$.

We assume that the artificial operation satisfies the following two properties:

(a) the addition of the artificial forcing does not affect KHK equation (3) nor Lin equation (5), i.e., these equations remain unchanged by the addition of $\boldsymbol{f}_a$ to Eq. (1), and
(b) it neither affects the terms representing the external force in Eqs. (3) and (5).

Among various possible options for $\boldsymbol{f}_a$ that satisfy (a) and (b), we use here $\boldsymbol{f}_a$ such that

$$\hat{\boldsymbol{f}}_a(\boldsymbol{k}) = \begin{cases} \mathrm{i}C\dfrac{\boldsymbol{k}}{|\boldsymbol{k}|} \times \hat{\boldsymbol{u}}(-\boldsymbol{k}) & (\text{in D}), \\ 0 & (\text{otherwise}), \end{cases} \tag{10}$$

where

$$D = \{\boldsymbol{k}\,|k_n - 1/2 \le k < k_n + 1/2, \quad (n = 0, 1, 2, \ldots, M)\},$$

the symbol i denotes the imaginary unit, and C is a real constant. The wavenumber k_n is given by $k_n = k_a + \alpha n$ for $n = 0, 1, 2, \ldots, M$, where $\alpha(\ge 1)$ and k_a are real constants, M is the maximum integer satisfying $k_M < k_{\max}$ (see Fig. 1), and $k_{\max}$ is the maximum wavenumber of the Fourier modes retained in the numerical simulation.

It is readily confirmed that the artificial forcing $\boldsymbol{f}_a$ given by Eq. (10) satisfies (I) the reality condition $\hat{\boldsymbol{f}}_a^*(\boldsymbol{k}) = \hat{\boldsymbol{f}}_a(-\boldsymbol{k})$, (II) the divergence free condition $\nabla \cdot \boldsymbol{f}_a = 0$, i.e., $\boldsymbol{k} \cdot \hat{\boldsymbol{f}}_a(\boldsymbol{k}) = 0$, and (III) $\hat{\boldsymbol{f}}_a(-\boldsymbol{k}) \cdot \hat{\boldsymbol{u}}(\boldsymbol{k}) = 0$, in which $\hat{\boldsymbol{f}}_a^*(\boldsymbol{k})$ denotes the complex conjugate of $\hat{\boldsymbol{f}}_a(\boldsymbol{k})$. Condition (III) ensures (a) and (b) because

$$\langle \boldsymbol{u}(\boldsymbol{r}+\boldsymbol{x}) \cdot \boldsymbol{f}_a(\boldsymbol{x}) + \boldsymbol{u}(\boldsymbol{x}) \cdot \boldsymbol{f}_a(\boldsymbol{r}+\boldsymbol{x}) \rangle = \iiint d\boldsymbol{k} \{\hat{\boldsymbol{f}}_a(-\boldsymbol{k}) \cdot \hat{\boldsymbol{u}}(\boldsymbol{k}) + \text{c.c.}\} \exp(\mathrm{i}\boldsymbol{k} \cdot \boldsymbol{r}) = 0,$$

where c.c. denotes the complex conjugate of the preceding term.

In order to get some idea on the role of $\boldsymbol{f}_a$, it may be instructive to consider the extreme limit in which the terms other than $\boldsymbol{f}_a$ are negligible in Eq. (1). We then have

$$\frac{\partial \hat{\boldsymbol{u}}(\boldsymbol{k})}{\partial t} = \begin{cases} \mathrm{i}C\dfrac{\boldsymbol{k}}{|\boldsymbol{k}|} \times \hat{\boldsymbol{u}}(-\boldsymbol{k}) & (\text{in D}), \\ 0 & (\text{otherwise}). \end{cases} \tag{11}$$

This implies that $\hat{\boldsymbol{u}}(\boldsymbol{k})$ outside D is unchanged by $\boldsymbol{f}_a$, but

$$\frac{\partial^2 \hat{\boldsymbol{u}}(\boldsymbol{k})}{\partial t^2} = -C^2 \hat{\boldsymbol{u}}(\boldsymbol{k}) \quad \text{in D}. \tag{12}$$

Equation (12) means that the Fourier modes in D propagate with the constant wave speed C independent of the wave vector $\boldsymbol{k}$ without changing their amplitudes. Thus, the introduction of the artificial forcing $\boldsymbol{f}_a$ may be understood as shifting the phases of the Fourier modes in D, or equivalently translating the waves with a constant speed, in a certain sense without changing their amplitudes.

The forcing $\hat{\boldsymbol{f}}_a(\boldsymbol{k})$ produces no energy but shifts the phase of each of $\hat{\boldsymbol{u}}(\boldsymbol{k})$'s. As is well known, the loss of phase coherence of $\hat{\boldsymbol{u}}(\boldsymbol{k})$ results in the loss of coherent structures.

In our simulations, these two fields, T- and F-fields, were generated by solving Eqs. (1) and (2) by using an alias-free Fourier spectral method with the number of grid points $N^3 = 512^3$ and a fourth-order Runge-Kutta method for time integration. The aliasing errors are removed by a phase shift method. Only the modes with wavenumbers satisfying $k \le k_{\max}$ are retained, where $k_{\max}$ is the maximum integer smaller than $2^{1/2}N/3$. The wavenumber increment is 1, and the minimum wavenumber is 1. The kinematic viscosity, $\nu = 3.0 \times 10^{-4}$, and the time increment Δt is taken to be equal to 1.0×10^{-3}.

Prior to the simulations of the T- and F-fields, say run T and run F, respectively, we performed another simulation starting at $t = 0$ with an initial random field whose energy spectrum is proportional to $k^4 \exp(-k^2/2)$ and total energy is 0.5. The field was developed until a certain time, say time $t = t_s \simeq 5\tau_L$, at which the mean energy dissipation rate per unit mass $\langle \epsilon \rangle$ was confirmed to be quasi-stationary, and the Taylor scale Reynolds number is $R_\lambda = 260$. Here, τ_L is L/u' at $t = t_s$, with L being the integral length scale defined by $L \equiv \pi/(2u'^2) \int_0^{k_{\max}} E(k)/k \, dk$, and R_λ is given by $R_\lambda \equiv u'\lambda/\nu$, with $\lambda \equiv (15\nu u'^2/\langle \epsilon \rangle)^{1/2}$.

Run T and run F were started by using this field at $t = t_s$ as their initial conditions. The simulations were carried out until $t = t_f$, where $t_f \simeq t_s + 2\tau_L$. As regards the artificial forcing $\boldsymbol{f}_a$ in run F, we used Eq. (10) with $C = 40 \simeq 8.0 \times 10/\tau_L = 2.4/\tau_K$, $\alpha = 4$, and $k_a = 48$ after some trials, where $k_a\eta = 0.2$, and τ_K is the Kolmogorov time scale at $t = t_s$. As the modulus of C increases, or as α or k_a decreases, the small-scale dynamics and structure are more destroyed, and the influence of $\hat{\boldsymbol{f}}_a$ on turbulence statistics at large scales becomes more significant.

Some of key statistics of the runs are shown in Table I. It is seen that the statistics for the T- and F-fields are similar to each other at $t = t_f$. It was observed that while $\langle \epsilon \rangle$ in run T is almost stationary during the entire simulation period, $\langle \epsilon \rangle$ in run F drops to approximately 10% of $\langle \epsilon \rangle$ of run T at an early stage $t - t_s \lesssim 0.2\tau_L$, but then it is recovered and becomes quasi-stationary after $t - t_s \gtrsim 0.8\tau_L$. Note that the constant $c(t)$ in the external forcing $\boldsymbol{f}$ given by Eq. (9) is so adjusted at every time step that the forcing compensates the energy dissipation by the viscosity. Therefore, the forcing $\boldsymbol{f}$ at the large scales with $k \lesssim k_F$ need not be the same in run T and run F. In order to check the effect of time increment, we performed simulation with the time increment decreased from Δt to $\Delta t/2$ in run F and confirmed that the difference is not significant. We also performed simulations, run T and run F, over

TABLE I. Turbulent statistics.

	R_λ	$\langle \epsilon \rangle$	L	λ	$\eta(\times 10^{-3})$
Initial field at $t = t_s$	260	0.0822	1.14	0.135	4.26
Run T at $t = t_f$	274	0.0742	1.21	0.142	4.37
Run F at $t = t_f$	274	0.0741	1.20	0.142	4.37

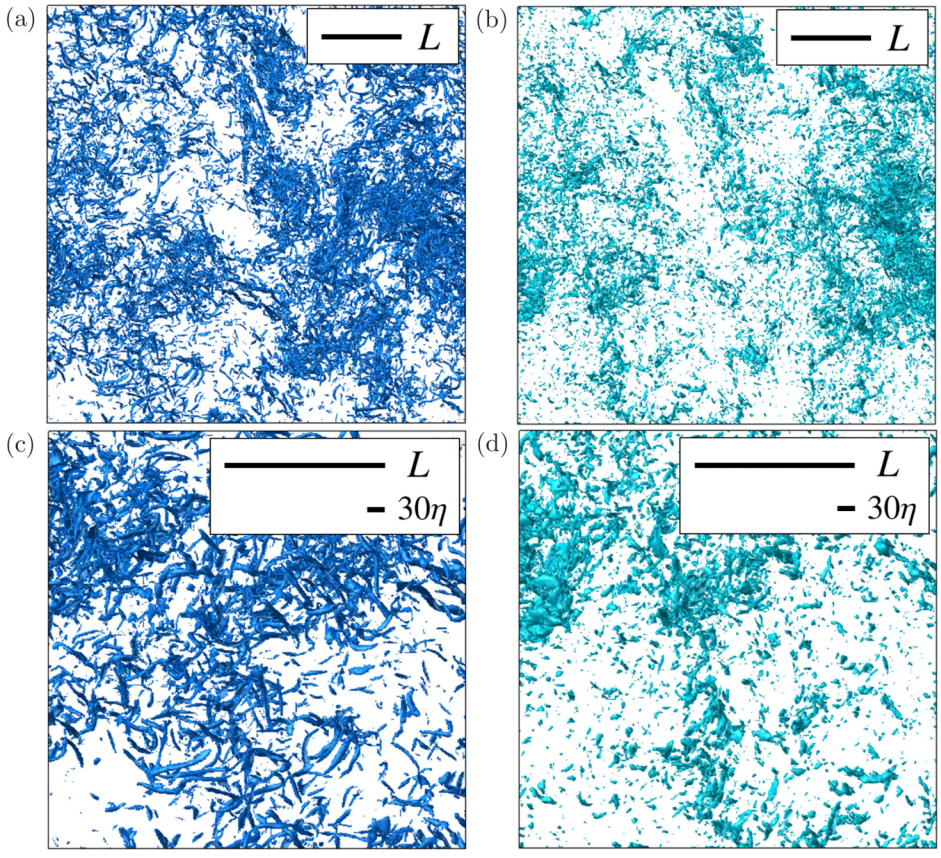

FIG. 2. Visualization of intense vorticity regions. The isosurfaces at $|\boldsymbol{\omega}| = m_\omega + 3\sigma_\omega$ in the 1/4 slice of the entire domain of the T- and F-fields are plotted in (a) and (b), respectively. Their zoom up views in a 1/4 sub-domain are presented in (c) and (d), respectively. Here, m_ω is the mean value of $|\boldsymbol{\omega}|$, and σ_ω is the standard deviation of $|\boldsymbol{\omega}|$. The isosurface value for the T-field is larger than that for the F-field.

a longer time period, until the time $t_f + 2\tau_L$, and confirmed that it does not give rise any significant change in the results presented in Sec. III.

III. NUMERICAL RESULTS

A. Visualization of vorticity

Some intuitive idea on the similarity and difference between the two fields may be obtained by visualization of the simulated fields. Figures 2(a) and 2(b) show the intense vorticity regions in the 1/4 slice of the entire domain of the fundamental periodic box of run T and run F, respectively. Figures 2(c) and 2(d) show their zoom up views in a 1/4 sub-domain of the slice.

In Figs. 2(a) and 2(c), it is observed that tube-like structures are formed by the NS dynamics in the T-field, as is well-known in previous studies (see, e.g., Refs. 5 and 6 for DNS observation and Ref. 7 for experimental observation). The comparison of the two fields in Figs. 2(a) and 2(b) shows that the field structures of run T and run F are similar to each other at large scales $\sim L$. However, their structures are distinctively different at smaller scales $\lesssim 30\eta$ ($\sim 2\pi/k_a$) as seen in Figs. 2(c) and 2(d). The vortex tube-like structures observed in Fig. 2(b) for the T-field are seen to be lost in Fig. 2(d) for the F-field. These observations hold for isosurfaces at higher $|\boldsymbol{\omega}|$ of each field; $|\boldsymbol{\omega}| = m_\omega + 5\sigma_\omega$ and $|\boldsymbol{\omega}| = m_\omega + 10\sigma_\omega$, where m_ω is the mean value of $|\boldsymbol{\omega}|$, and σ_ω is the standard deviation of $|\boldsymbol{\omega}|$.

The difference at small scales does not imply substantial change of the enstrophy, as seen in the fact that $\langle\epsilon\rangle$ of the T-field is in good agreement with that of the F-field (see Table I). This is consistent with the conjecture that $\langle\epsilon\rangle$ is mainly determined by the dynamics in the energy containing range.

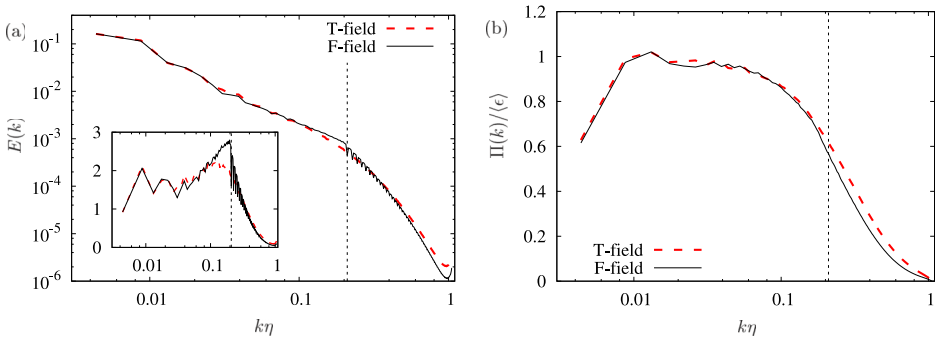

FIG. 3. (a) Energy spectra $E(k)$ vs. $k\eta$. The inset of (a) shows $k^{5/3}E(k)/\langle\epsilon\rangle^{2/3}$ vs. $k\eta$. (b) Normalized energy flux $\Pi(k)/\langle\epsilon\rangle$ vs. $k\eta$. The dotted lines show $k\eta = k_a\eta = 0.2$.

B. Energy spectra and energy flux

The similarity at large scales and the difference at small scales between the two fields, T- and F-fields, are also seen in their energy spectra $E(k)$. Figure 3(a) shows $E(k)$ of the two fields, and its inset shows the compensated energy spectra, where $E(k)$ was computed by

$$E(k) = \frac{1}{2} \sum_{k-1/2 \le |\boldsymbol{\kappa}| < k+1/2} |\hat{\boldsymbol{u}}(\boldsymbol{\kappa})|^2 \tag{13}$$

from the simulated data of $\hat{\boldsymbol{u}}(\boldsymbol{k})$.

It is seen that the spectra are close to each other at small dimensionless wavenumber range $k\eta \lesssim 0.1$, but they are a little different at larger dimensionless wavenumbers $k\eta \gtrsim 0.2$. The difference is clearly visible in the compensated energy spectra in the inset. A sharp increase of the compensated spectrum for the F-field, in contrast to the T-field, is observed at $k\eta \sim 0.2$.

This enhancement is consistent with smallness of the energy flux $\Pi(k)$ in the F-field as compared to that in the T-field, as seen in Fig. 3(b) where $\Pi(k)$ was evaluated by $\Pi(k) = -\sum_{\kappa=1}^{k} T_E(\kappa)$ with the energy transfer function $T_E(\kappa)$ being computed in the same way as in Eq. (13). The smallness of energy transfer in run F as compared to run T at $k\eta \gtrsim 0.2$ is consistent with the conjecture that the transfer is suppressed by the destruction or loss of the smaller-scale coherent structures in the F-field. In spite of the difference in $E(k)$ and $\Pi(k)$ of the two fields at the smaller scales at $k\eta \gtrsim 0.2$, they are similar to each other at larger scales, $k\eta \lesssim 0.1$.

C. Energy transfer

An essence of turbulence dynamics lies in the energy transfer between different scales. A quantitative measure characterizing this transfer is given by

$$T \equiv -\tau_{ij}\overline{S}_{ij},$$

where

$$\tau_{ij} = \left(\overline{u_i u_j} - \overline{u}_i\,\overline{u}_j\right) - \frac{2}{3}\delta_{ij}q, \quad q = \frac{1}{2}\left(\overline{u_\ell u_\ell} - \overline{u}_\ell\,\overline{u}_\ell\right), \quad \text{and} \quad \overline{S}_{ij} = \frac{1}{2}\left(\frac{\partial \overline{u}_i}{\partial x_j} + \frac{\partial \overline{u}_j}{\partial x_i}\right),$$

in which the summation convention for repeated indices is used, δ_{ij} is the Kronecker delta, the overbar $\bar{}$ denotes the filtering operation defined by $\hat{\overline{h}}(\boldsymbol{k}) = G(\boldsymbol{k})\hat{h}(\boldsymbol{k})$, and $G(\boldsymbol{k})$ is the Fourier transform of a filtering function.

We used two kinds of filters. One is the so-called spectral cut filter by which all the Fourier modes with wavenumbers k larger than the cutoff wavenumber k_c are removed, i.e., $G(\boldsymbol{k}) = 1$ for $k < k_c$ and $= 0$ for $k \ge k_c$, and the other is the so-called Gaussian filter in which $G(k)$ is given by $G(k) = \exp[-\pi^2 k^2/(24k_c^2)]$. The above definition of the transfer T is the same as that in previous studies, e.g., Refs. 8–10. See, for example, Ref. 10 which shows statistics of T in high solution DNS of isotropic turbulence with R_λ up to 1132.

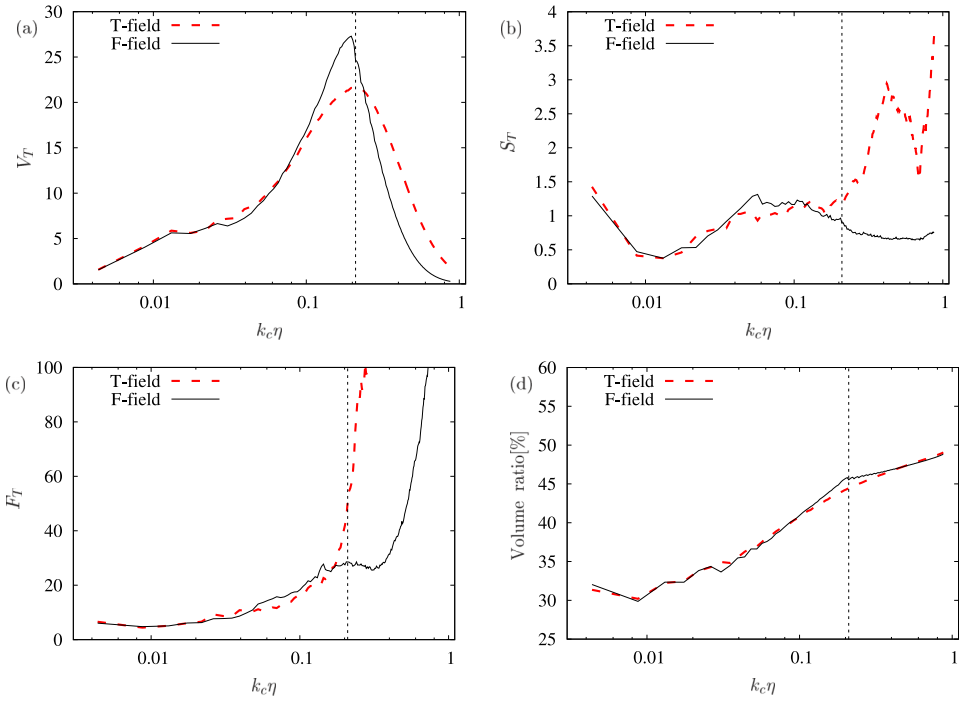

FIG. 4. $k_c\eta$-dependence of statistics on the energy transfer $T(k_c)$; (a) the dimensionless variance V_T, (b) the skewness S_T, (c) the flatness F_T, and (d) the volume ratio of the negative values of T. The dotted lines show $k_c\eta = k_a\eta = 0.2$.

Note that $T = T(k_c,\boldsymbol{x})$ is a function of the position $\boldsymbol{x}$ as well as of the cutoff wavenumber k_c. If $T > 0$, then the energy is transferred from larger scale with $k < k_c$ to smaller scale with $k \geq k_c$ while if $T < 0$, it is transferred from smaller to larger scales. They are called forward transfer and backward transfer, respectively.

In the following, we present results only under the use of the spectral cut filter, unless otherwise stated. Under the use of the spectral cut filter, we have

$$\langle T(k)\rangle = \Pi(k), \tag{14}$$

where the brackets $\langle\,\rangle$ denote the volume average over the fundamental periodic domain. Equality (14) was confirmed in our numerical analysis with $k_c = n + 1/2$ ($n = 1,2,\ldots$).

Figures 4(a)–4(c), respectively, show the dimensionless variance $V_T \equiv \left\langle (T - \langle T\rangle)^2\right\rangle / \langle\epsilon\rangle^2$, the skewness S_T of T, the flatness F_T of T, and the volume ratio of the backscatter, as a function of the cutoff filtering wavenumber k_c. It is seen in Fig. 4 that the statistics of the two fields, T- and F-fields, are similar to each other at the wavenumber range $k\eta \lesssim 0.1$, but different at larger $k\eta$. This implies that in spite of the loss in the F-field of the structures that were formed in the T-field by the true NS dynamics, the statistics of the energy transfer T at the larger scales remain almost unchanged. This is true not only for the average but also for the higher-order statistics of T, as seen in Figs. 4(a)–4(c). The volume ratio of backscatter regions at the larger scales is neither affected significantly by the loss, as seen in Fig. 4(d).

These results were confirmed to hold also under the use of the Gaussian filter (figure omitted). They suggest that the energy transfer at larger scales is not sensitive to the small-scale structures such as the vortex tubes.

D. Probability distribution functions (PDFs) of vorticity

As is well-known, fully developed turbulent flows at high Reynolds number exhibit strong intermittency, especially in the dissipation range. The intermittency is manifested by the PDF of, for

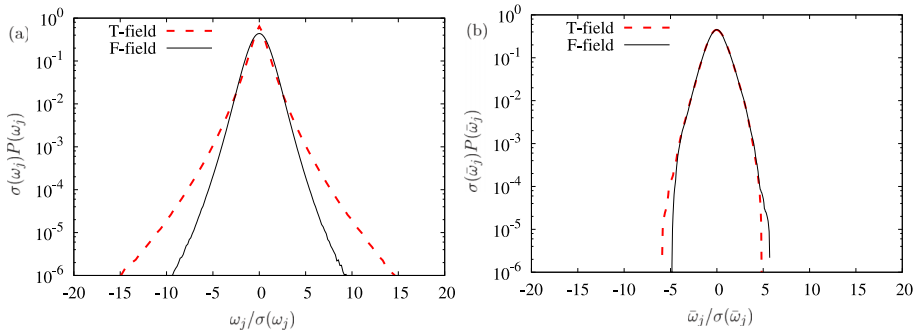

FIG. 5. Normalized PDFs of a vorticity component ω_j and coarse-grained one $\bar{\omega}_j$ with $k_c\eta = 0.04$. Here, $\sigma(\cdot)$ is the standard deviation of $\cdot$.

example, a vorticity component ω_j, as shown in Fig. 5(a) for the two original fine fields, the fine T- and F-fields.

It is seen that the PDF for the T-field has a wide skirt, corresponding to the strong intermittency in the dissipation range. In contrast, the skirt of the PDF for the F-field is seen to be much narrower. The intermittency is much weaker in the F-field than in the T-field. It is presumably suppressed by the loss of the coherent structures at the small scales due to the computational surgery.

Figure 5(b) shows the PDFs of $\bar{\omega}_j$ for the T- and F-fields, where $\bar{\omega}_j$ is a coarse-grained vorticity component, in which k_c is taken to be 9.5 ($k_c\eta = 0.04$ at $t = t_f$), as a representative wavenumber of large scales. We see that the PDF for the F-field agrees well with that for the T-field. This implies that the PDF of the coarse-grained vorticity is almost unaffected by the computational surgery or the loss of the coherent structures at the small scales $\sim\eta$.

E. Geometry

We examine the influence of the small-scale vortex dynamics and structures on larger scale statistical geometry of turbulence. Among various measures characterizing the geometry are the alignment of the vorticity and eigenvectors of the rate-of-strain tensor S_{ij}, and the local flow topology characterized by the two invariants of velocity gradient tensor $A_{ij} = \partial u_i/\partial x_j$ satisfying $A_{ii} = 0$ (see, e.g., a review article[11]).

1. *Alignment of vorticity and eigenvectors of rate-of-strain tensor*

Since the tensor S_{ij} is symmetric and traceless, it has three real eigenvalues, say $\lambda_\ell(\ell = 1,2,3)$ satisfying $\lambda_1 + \lambda_2 + \lambda_3 = 0$, where we may put $\lambda_1 \le \lambda_2 \le \lambda_3$ without loss of generality, so that $\lambda_1 < 0$ and $\lambda_3 > 0$. A quantitative measure of the alignment is given by

$$\cos\theta_\ell = \frac{\boldsymbol{\omega}\cdot\boldsymbol{e}_\ell}{|\boldsymbol{\omega}||\boldsymbol{e}_\ell|}, \tag{15}$$

where $\boldsymbol{e}_\ell$ is the eigenvectors corresponding to λ_ℓ.

Figure 6(a) shows the PDFs of $\cos\theta_\ell$ for the fine T- and F-fields. The PDFs for the T-field agree with those in, e.g., Refs. 12–14. The PDFs at $\ell = 1,2,3$ for the F-field are, respectively, flatter, than those for the T-field. We conjecture that this is attributed to weak vorticity in the F-field compared to that in the T-field (see Figs. 2 and 5(a)). Indeed, Vincent and Meneguzzi[15] show that the PDFs of the alignment between $\boldsymbol{e}_\ell$ and weak vorticity are flatter than those of the alignment between $\boldsymbol{e}_\ell$ and intense vorticity. It is also seen that both fields exhibit the existence of preferential alignment between intermediate eigenvector and vorticity. This suggests that the alignment is not lost by the loss of the small-scale structures.

Figure 6(b) shows the PDFs of $\cos\theta_\ell$ for the coarse-grained T- and F-fields, where the fields $\boldsymbol{\omega}$ and $\boldsymbol{e}_\ell$ in Eq. (15) are replaced by the corresponding vectors obtained by the use of the coarse-grained velocity fields filtered with $k_c\eta = 0.04$. It is seen that the difference between the

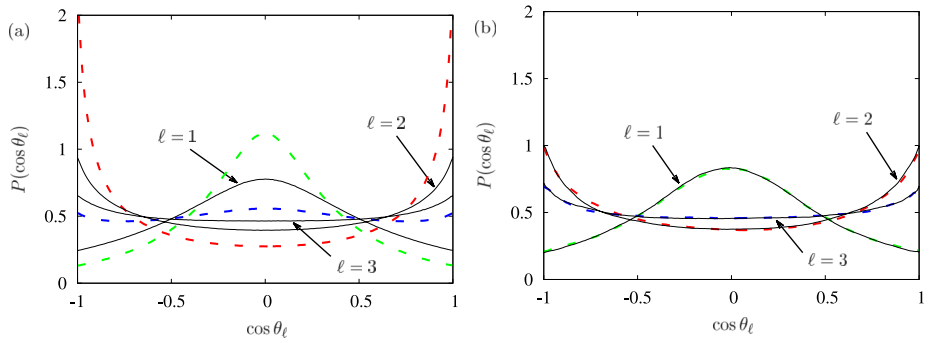

FIG. 6. PDFs of $\cos\theta_\ell$ ($\ell = 1, 2, 3$) for (a) the fine fields and (b) the coarse-grained fields with $k_c\eta = 0.04$. The green, red, and blue dashed lines show the PDFs for $\ell = 1, 2, 3$ in the T-field, respectively while the black solid lines, pointed by the arrows with $\ell = 1, 2, 3$, express the PDFs of $\cos\theta_\ell$ in the F-field.

PDFs for the coarse-grained T- and F-fields is very small. This suggests that the alignment of the coarse-grained vorticity and the eigenvectors of the coarse-grained rate-of-strain tensor is little affected by the loss of the small-scale structures.

2. Joint PDFs of invariants of velocity gradient tensor

The two invariants of the velocity gradient tensor A_{ij}, i.e., the second and third invariants, Q and R, are defined as

$$Q = -\frac{1}{2}A_{ij}A_{ji}, \tag{16}$$

$$R = -\frac{1}{3}A_{ij}A_{j\ell}A_{\ell i}. \tag{17}$$

The field has four non-degenerate local flow topologies:[16] unstable focus-compressing pattern ($R > 0$ and $Q^3 > 27R^2/4$), stable focus-stretching pattern ($R < 0$ and $Q^3 > 27R^2/4$), stable node-saddle-saddle pattern ($R < 0$ and $Q^3 < 27R^2/4$), and unstable node-saddle-saddle pattern ($R > 0$ and $Q^3 < 27R^2/4$).

Figure 7(a) shows the joint PDFs of the dimensionless invariants for the two fine fields. Both of the PDFs present teardrop shapes. We observe the predominance of the stable focus-stretching and

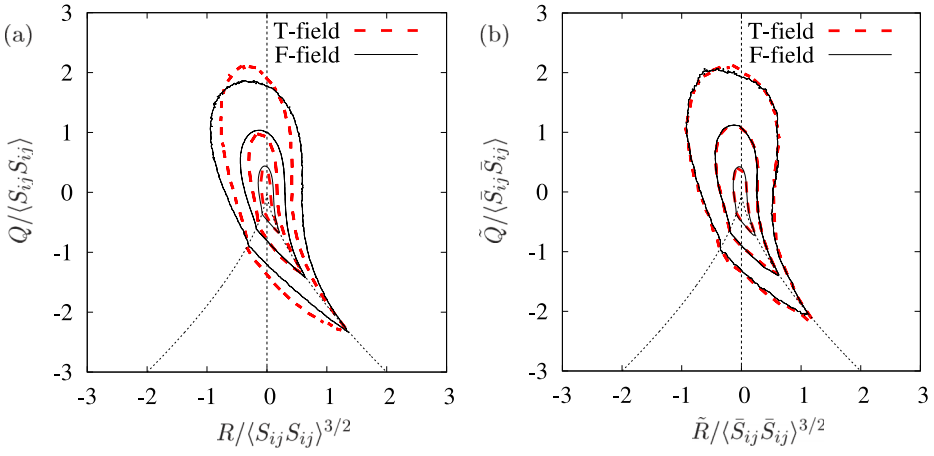

FIG. 7. Joint PDFs of (a) the dimensionless invariants $Q/\langle S_{ij}S_{ij}\rangle$ and $R/\langle S_{ij}S_{ij}\rangle^{3/2}$ for the fine fields, and (b) $\tilde{Q}/\langle \bar{S}_{ij}\bar{S}_{ij}\rangle$ and $\tilde{R}/\langle \bar{S}_{ij}\bar{S}_{ij}\rangle^{3/2}$ for the coarse-grained fields with $k_c\eta = 0.04$. Contour lines in all cases are logarithmically spaced by a factor 10 as 1, 10^{-1}, and 10^{-2}, starting near the origin. The dotted lines represent $27R^2/4 + Q^3 = 0$ in (a) and $27\tilde{R}^2/4 + \tilde{Q}^3 = 0$ in (b) while the thin dashed ones show $R = 0$ and $\tilde{R} = 0$.

unstable node-saddle-saddle patterns over the others, as reported in previous studies.[14,17] The joint PDF for the F-field is much broader than that for the T-field. We see that the F-field exhibits the predominance.

Figure 7(b) shows the joint PDFs of the invariants for the coarse-grained T- and F-fields $\bar{\boldsymbol{u}}$ with larger scale $k_c\eta = 0.04$. We use $\bar{\boldsymbol{u}}$ instead of $\boldsymbol{u}$ in Eqs. (16) and (17), and the invariants for $\bar{\boldsymbol{u}}$ are written as $\tilde{Q}$ and $\tilde{R}$. It is seen in Fig. 7(b) that the PDFs for the coarse grained T- and F-fields, in contrast to those for the fine T- and F-fields in Fig. 7(a), are similar to each other, where the values of normalization factor $\langle \bar{S}_{ij}\bar{S}_{ij}\rangle$ for the T- and F-fields in Fig. 7(b) are similar to each other, and the same is also the case for $\langle S_{ij}S_{ij}\rangle$ in Fig. 7(a). This suggests that the statistics of flow topology is robust against the loss of the small-scale structures.

IV. DISCUSSION AND CONCLUSION

In order to get some idea on the role of the exact dynamics and structure at small scales in high Reynolds number turbulence, we have compared in this study two fields. One is the true field or the T-field, and the other is the false field or the F-field. The T-field was generated by DNS of an incompressible turbulent field obeying the NS equation under periodic boundary conditions and external forcing confined only at small wavenumbers. The F-field was generated by introducing an artificial computational operation, i.e., computational surgery, to the T-field. The surgery destroys the small-scale dynamics and structures formed by the NS dynamics in the T-field. In the F-field, the phases of some Fourier modes at high wavenumber are shifted by the operation, i.e., the modes are translated in space without changing their amplitudes by the surgery.

The KHK equation and the Lin equation for the F-field are identical to those for the T-field (see the two properties of artificial operations (a) and (b) in Sec. II B). Moreover, the boundary conditions and the initial conditions are the same for these two fields. These coincidences, however, do not imply the coincidence of the two fields as could be expected. As a matter of fact, the tube-like structures of high vorticity regions observed in the T-field are lost in the F-field.

This implies a difficulty of closure models or the so-called spectral closures that involve only second-order moments, because it would be difficult for these models or closures to distinguish the two fields.

On the other hand, it is also seen in the numerical results presented in Sec. III that in spite of the differences observed at scales ($\sim\eta$), the statistics of the two fields are similar to each other at larger scales ($\gg\eta$). This implies that the statistics at the large scales are insensitive to the difference at the small scales. It is in agreement with the conjecture that the inertial range structures are determined primarily by the dynamics in the range, and the exact dynamics and structures in the dissipation range play only a secondary role in the determination, provided that the energy is transferred to small scales appropriately. One might conjecture from this that the similar may be true for systems that obey a certain dynamics different from the NS dynamics at small scales, but similar one at larger scales. Among them is superfluid turbulence.[18,19]

The insensitivity of large-scale statistics to the difference of the small-scale dynamics and structure is quite encouraging to the modeling or closures noted above, as well as to large eddy simulation, which is based on the assumption that the large-scale statistics are not sensitive to the details of the small-scale dynamics and structure.

It is encouraging also to the use of the eddy viscosity models, behind which is presumably the idea that large-scale statistics are not sensitive to the exact dynamics and structure at small scales. It would be interesting to study the influence of the use of the eddy viscosity model on the statistics. In this paper, we confined ourselves only to the operation satisfying two conditions (a) and (b) discussed in Sec. II, in contrast to eddy viscosity models by which (a) and (b) should be modified. Such study is outside the scope of this paper and remained to be pursued, but readers may refer to, e.g., pioneering studies by Refs. 20 and 21.

The suggestion implied by our numerical results that the small-scale dynamics plays only a secondary role is also consistent with the study by Yoshida *et al.*[22] which shows that even if

small-scale information was lost at some instant, it can be re-generated under a certain conditions, provided that large-scale information is kept appropriately.

In conclusion, it is fair to note that our preliminary study suggests that if the artificial forcing due to the operation is too strong, then the statistics of T- and F-fields are quite different from each other at large scales. This suggests that if the forcing is too strong, then the small-scale structures may be so much destroyed that the energy transfer is affected significantly.

ACKNOWLEDGMENTS

The authors are grateful to Professor P. Davidson for the valuable comments on the role of the vortex structure on the energy transfer. They also thankfully acknowledge fruitful discussions on this work at the international academic network meeting on "Waves and Turbulence in Rotating, Stratified and Electrically Conducting Fluids" supported by the Leverhulme Trust. The computations were carried out on the FX10 systems at the Information Technology Center of Nagoya University. This work was partly supported by JSPS KAKENHI Grant Nos. (S) 24224003 and (C) 25390149.

[1] Y. Kaneda, T. Ishihara, M. Yokokawa, K. Itakura, and A. Uno, "Energy dissipation rate and energy spectrum in high resolution direct numerical simulations of turbulence in a periodic box," Phys. Fluids **15**, L21–L24 (2003).
[2] A. N. Kolmogorov, "Dissipation of energy in the locally isotropic turbulence," Dokl. Akad. Nauk SSSR **32**, 16–18 (1941), reprinted in Proc. R. Soc. A **434**, 15–17 (1991).
[3] Y. Kaneda and K. Morishita, "Small-scale statistics and structure of turbulence—In the light of high resolution direct numerical simulation," in *Ten Chapters in Turbulence*, edited by P. A. Davidson, Y. Kaneda, and K. R. Sreenivasan (Cambridge University Press, Cambridge, 2013), pp. 1–42.
[4] U. Frisch, *Turbulence* (Cambridge University Press, Cambridge, 1995).
[5] J. Jiménez, A. A. Wray, P. G. Saffman, and R. S. Rogallo, "The structure of intense vorticity in isotropic turbulence," J. Fluid Mech. **255**, 65–90 (1993).
[6] E. D. Siggia, "Numerical study of small-scale intermittency in three-dimensional turbulence," J. Fluid Mech. **107**, 375–406 (1981).
[7] S. Douady, Y. Couder, and M. E. Brachet, "Direct observation of the intermittency of intense vorticity filaments in turbulence," Phys. Rev. Lett. **67**, 983–986 (1991).
[8] U. Piomelli, T. A. Zang, C. G. Speziale, and M. Y. Hussaini, "On the large-eddy simulation of transitional wall-bounded flows," Phys. Fluids A **2**, 257–265 (1990).
[9] J. A. Domaradzki, W. Liu, and M. E. Brachet, "An analysis of subgrid-scale interactions in numerically simulated isotropic turbulence," Phys. Fluids A **5**, 1747–1759 (1993).
[10] T. Aoyama, T. Ishihara, Y. Kaneda, M. Yokokawa, K. Itakura, and A. Uno, "Statistics of energy transfer in high-resolution direct numerical simulation of turbulence in a periodic box," J. Phys. Soc. Jpn. **74**, 3202–3212 (2005).
[11] J. M. Wallace, "Twenty years of experimental and direct numerical simulation access to the velocity gradient tensor: What have we learned about turbulence?," Phys. Fluids **21**, 021301 (2009).
[12] A. Tsinober, E. Kit, and T. Dracos, "Experimental investigation of the field of velocity gradient in turbulent flows," J. Fluid Mech. **242**, 169–192 (1992).
[13] Wm. T. Ashurst, A. R. Kerstein, R. M. Kerr, and C. H. Gibson, "Alignment of vorticity and scalar gradient with strain rate in simulated Navier–Stokes turbulence," Phys. Fluids **30**, 2343–2353 (1987).
[14] L. Chevillard, C. Meneveau, L. Biferale, and F. Toschi, "Modeling the pressure Hessian and viscous Laplacian in turbulence: Comparisons with direct numerical simulation and implications on velocity gradient dynamics," Phys. Fluids **20**, 101504 (2008).
[15] A. Vincent and M. Meneguzzi, "The dynamics of vorticity tubes in homogeneous turbulence," J. Fluid Mech. **258**, 245–254 (1994).
[16] M. S. Chong, A. E. Perry, and B. J. Cantwell, "A general classification of three-dimensional flow fields," Phys. Fluids A **2**, 765–777 (1990).
[17] J. Soria, R. Sondergaard, B. J. Cantwell, M. S. Chong, and A. E. Perry, "A study of the fine-scale motions of incompressible time-developing mixing layers," Phys. Fluids **6**, 871–884 (1994).
[18] J. Maurer and P. Tabeling, "Local investigation of superfluid turbulence," Europhys. Lett. **43**, 29–34 (1998).
[19] J. Salort, C. Baudet, B. Castaing, B. Chabaud, F. Daviaud, T. Didelot, P. Diribarne, B. Dubrulle, Y. Gagne, F. Gauthier, A. Girard, B. Hébral, B. Rousset, P. Thibault, and P.-E. Roche, "Turbulent velocity spectra in superfluid flows," Phys. Fluids **22**, 125102 (2010).
[20] V. Borue and S. A. Orszag, "Forced three-dimensional homogeneous turbulence with hyperviscosity," Europhys. Lett. **29**, 687–692 (1995).
[21] N. E. L. Hagen and A. Brandenburg, "Inertial range scaling in numerical turbulence with hyperviscosity," Phys. Rev. E **70**, 026405 (2004).
[22] K. Yoshida, J. Yamaguchi, and Y. Kaneda, "Regeneration of small eddies by data assimilation in turbulence," Phys. Rev. Lett. **94**, 014501 (2005).